MATERIALS SCIENCE

Preserving surface strain in nanocatalysts via morphology control

Chuqiao Shi[1]†, Zhihua Cheng[2]†, Alberto Leonardi[3,4,5], Yao Yang[6], Michael Engel[4], Matthew R. Jones[1,2]*, Yimo Han[1]*

Engineering strain critically affects the properties of materials and has extensive applications in semiconductors and quantum systems. However, the deployment of strain-engineered nanocatalysts faces challenges, in particular in maintaining highly strained nanocrystals under reaction conditions. Here, we introduce a morphology-dependent effect that stabilizes surface strain even under harsh reaction conditions. Using four-dimensional scanning transmission electron microscopy (4D-STEM), we found that cube-shaped core-shell Au@Pd nanoparticles with sharp-edged morphologies sustain coherent heteroepitaxial interfaces with larger critical thicknesses than morphologies with rounded edges. This configuration inhibits dislocation nucleation due to reduced shear stress at corners, as indicated by molecular dynamics simulations. A Suzuki-type cross-coupling reaction shows that our approach achieves a fourfold increase in activity over conventional nanocatalysts, owing to the enhanced stability of surface strain. These findings contribute to advancing the development of advanced nanocatalysts and indicate broader applications for strain engineering in various fields.

INTRODUCTION

Engineering surface strain can improve the performance of nanocatalysts as it directly influences electronic states and active sites, offering the potential to design high-performance catalysts for a wide range of applications (*1*–*5*). Among the various methods to impart surface strain, the growth of core-shell nanostructures has emerged as a promising approach since it enables precise control of surface strain through lattice heteroepitaxy (*4*, *6*–*8*). However, the propensity of epitaxial strain to spontaneously relax through dislocation nucleation under operating conditions limits their utility. Consequently, the discovery of methods to trap metastable strain states in materials is desirable for improving their durability and performance.

Matthews and Blakeslee's (*9*) equilibrium theory of dislocation formation suggests that strain relaxation in heteroepitaxial growth begins when the film exceeds a certain critical thickness that occurs when the accumulated strain energy surpasses that required to create misfit dislocations. For core-shell metal nanoparticles (NPs), previous research has suggested a critical thickness of only a few monolayers, owing to the ease of forming misfit dislocations and stacking faults that release the surface strain (*10*–*13*). Thus, great synthetic effort has been devoted to the generation and maintenance of conformal, ultrathin heteroepitaxial shells that nonetheless tend to quickly relax due to their thermodynamic instability in operando, thereby rapidly losing their effectiveness (*5*, *14*–*19*). This is a particularly salient factor in strain-engineered catalytic systems which often require high temperatures and/or harsh reaction conditions to perform optimally.

In this work, we demonstrate that a sharp-edge morphology in the nanoparticle (NP) core effectively inhibits dislocation formation in the shell, thereby improving surface strain stability compared to their conventional rounded-core counterparts (Fig. 1A). We use core-shell Au_{cube}@Pd_{cube} particles as a model system (fig. S1), given the large but accommodatable mismatch of 4.8% between relaxed Au and Pd lattices (*11*). Atomic-resolution annular dark-field scanning transmission electron microscopy (ADF-STEM) images (Fig. 1B) depict core-shell Au_{cube}@Pd_{cube} NPs that represent the extremes of radius of curvature values of 4.4 and 18.5 nm at their corners. For the sharp-core Au NPs, the Pd shell forms a coherent interface, while those with rounded-cores show mismatch near the corners.

RESULTS

To understand the differences in strain states in these two cases, we quantify it via a high-precision whole-particle strain analysis using 4D-STEM. Different from conventional geometric phase analysis (*5*, *20*), which requires atomic-resolution images and typically offers a limited field of view with high noise, we use a nanobeam 4D-STEM approach (*21*, *22*), which affords us a remarkable (<0.18%) strain precision and allows for comprehensive mapping of entire particles over dimensions spanning from a few to hundreds of nanometers (Fig. 1C). Throughout the collection of 4D datasets, the electron probe scans across the core-shell Au_{cube}@Pd_{cube} NP, while the electron microscope pixel array detector (EMPAD) (*23*) records full diffraction patterns at each position (Fig. 1D, top). Although core-shell systems pose challenges in 4D data processing, including lattice misalignments and projection complexities arising from overlapped materials, we addressed them via optimized exit-wave power-cepstrum (EWPC) analysis (*24*) (Fig. 1D, bottom; with details in fig. S2 and Materials and Methods) and developing mismatch correction for the projected core (details in fig. S3 and Materials and Methods), respectively. These steps are essential in eliminating potential errors from the strain profile, ultimately yielding high-precision strain measurements spanning the entirety of the nanostructure.

[1]Department of Materials Science and NanoEngineering, Rice University, Houston, TX 77006, USA. [2]Department of Chemistry, Rice University, Houston, TX 77006, USA. [3]Diamond Light Source Ltd., Harwell Science and Innovation Campus, Didcot, Oxfordshire OX11 0DE, UK. [4]Institute for Multiscale Simulation, IZNF, Friedrich-Alexander-Universität Erlangen-Nürnberg, 91058 Erlangen, Germany. [5]Department of Earth and Atmospheric Sciences, Indiana University, 1001 East 10th Street, Bloomington, IN 47405, USA. [6]Department of Chemistry and Chemical Biology, Cornell University, Ithaca, NY 14850, USA.
*Corresponding author. Email: yimo.han@rice.edu (Y.H.); mrj@rice.edu (M.R.J.)
†These authors contributed equally to this work.

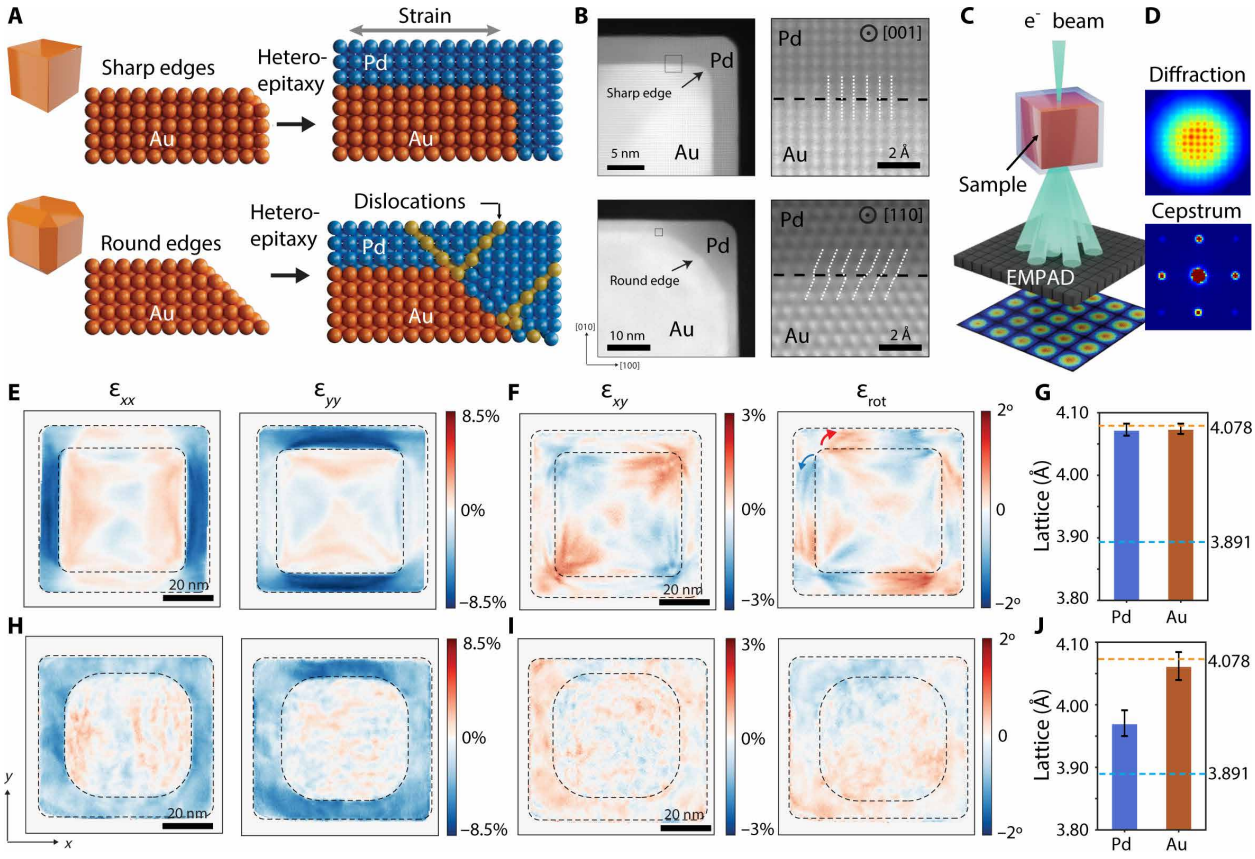

Fig. 1. Enhancing surface strain stability via nanoscale morphology control. (**A**) Schematic illustration of strain preservation by a nanoscale morphology with sharp edges. (**B**) Atomic-resolution ADF-STEM images of the sharp-core (top left) and round-core (bottom left) $Au_{cube}@Pd_{cube}$ NPs. Zoomed-in images from boxed area show a coherent interface (top right) and lattice mismatch (bottom right) between Au and Pd in sharp-core and round-core particles respectively, with the zone axes labeled. (**C** and **D**) Schematic showing 4D-STEM with a diffraction pattern (D, top) and an EWPC (D, bottom) from the core-shell NP for precise strain analysis. (**E**, **F**, **H**, and **I**) Strain maps (ε_{xx}, ε_{yy}, ε_{xy}, and ε_{rot}) from individual sharp-core (E and F) and round-core (H and I) $Au_{cube}@Pd_{cube}$ NPs. The red and blue arrows indicate clockwise and counterclockwise rotation, respectively. (**G** and **J**) Lattice parameters that are parallel to the interface between Au and Pd for sharp-core (G) and round-core (J) NPs.

The strain map for individual sharp-core $Au_{cube}@Pd_{cube}$ particles (Fig. 1, E and F) reveals a highly strained 8-nm Pd shell surrounding the Au core. Since the strain is calculated with respect to a perfect Au crystal as a reference, 0 and −4.8% correspond to the relaxed values of Au and Pd lattices, respectively. The measured lattice constants of Au and Pd along the interface are both close to the ideal Au lattice constant (statistics shown in Fig. 1G and calculation in fig. S4, A to C). Conversely, the Pd lattice undergoes compressive strain in the direction perpendicular to the interface due to the Poisson effect (as shown in fig. S5). This tetragonal lattice deformation in the Pd shell is best illustrated by calculating the lattice constant ratio a_x/a_y (as shown in fig. S6), where a_x and a_y are the lattice constants along x and y directions, respectively. Despite a similar shell thickness to the sharp-core $Au_{cube}@Pd_{cube}$ NPs, those with rounded cores show notable differences in the strain maps that indicate a release of tensile strain (Fig. 1, H and I), rendering the interface between the Au and Pd incoherent. In this case, the measured Pd shell lattice constant (3.970 Å) is 2.7% mismatched with Au and closer to the bulk value for Pd (statistics shown in Fig. 1J and calculation in fig. S4, D to F), suggesting strain relaxation. This conclusion is corroborated by maps of the off-diagonal components of the stress-strain tensor, which reveal substantial residual tangential shear and rotational effects for sharp-core $Au_{cube}@Pd_{cube}$ NPs (Fig. 1F), that are not present in the round-core $Au_{cube}@Pd_{cube}$ NPs (Fig. 1I). This further illustrates the sensitive dependence of strain preservation on particle core morphology in heteroepitaxial nanostructures.

To reveal the role of core sharpness on strain relaxation, we developed synthetic methods that allowed for the growth of $Au_{cube}@Pd_{cube}$ NPs with the same Pd shell thickness but different Au core tip curvatures. In brief, by increasing the bromide ion concentration during particle synthesis, growth along ⟨111⟩ directions can be accelerated, leading to the development of Au cubes with predominantly {100} facets and sharper tips (details in fig. S7 and Materials and Methods). We quantify Au core morphology using the sharpness index (SI) (*25*) (defined in fig. S8), which compares the tip radius of curvature to the edge length with values closer to one indicating sharper features. To precisely control Pd shell growth, we manipulated the quantity of Au cubes added to a Pd overgrowth solution (see Materials and Methods for more details). Careful control of these parameters allowed for the measurement of 4D-STEM strain profiles of $Au_{cube}@Pd_{cube}$ NPs with a range of Pd shell thicknesses across three Au core SI values (Fig. 2, A to C). The strain and lattice constant ratio maps represent the average of four edges from a single particle to reduce noise. For sharp-core $Au_{cube}@Pd_{cube}$

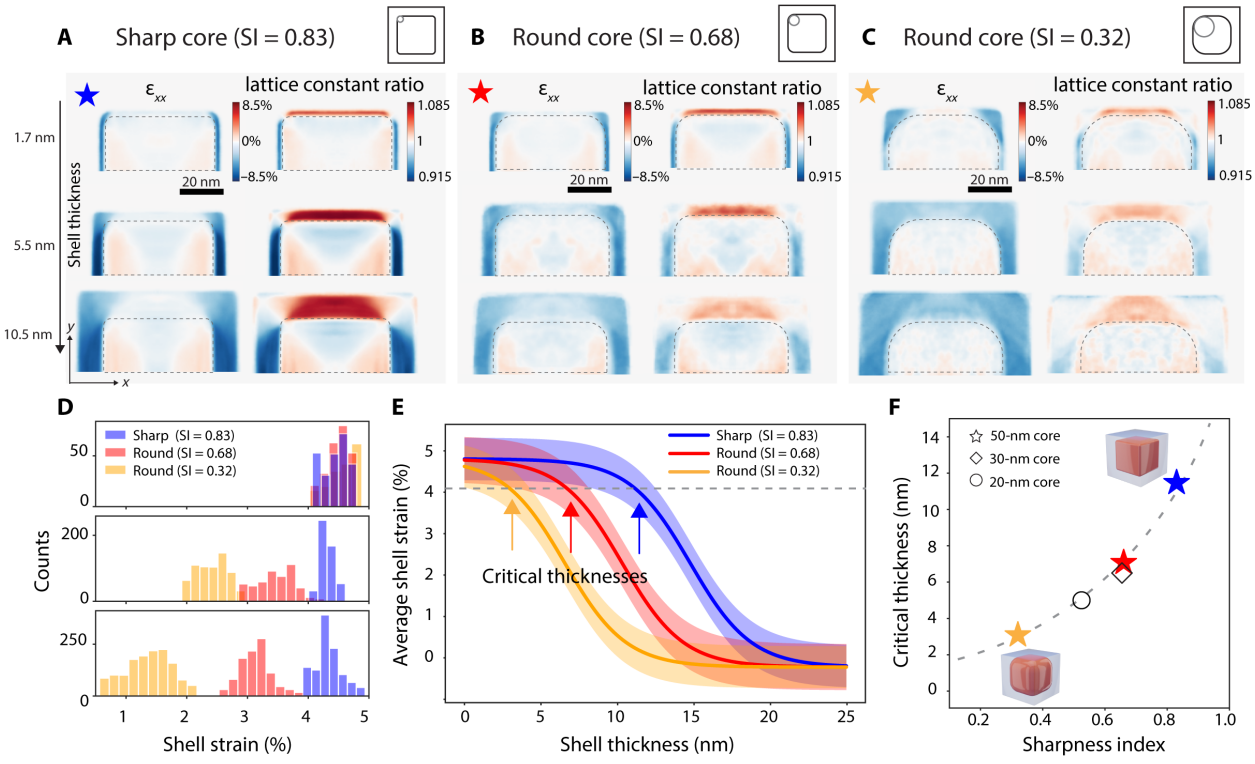

Fig. 2. Morphology-dependent critical thicknesses. (**A** to **C**) 4D-STEM strain maps (ε_{xx} with Au lattice as reference) and lattice-constant-ratio maps of the core-shell $Au_{cube}@Pd_{cube}$ particles with different shell thicknesses (top to bottom: 1.7 ± 0.3, 5.5 ± 0.5, and 10.5 ± 0.5 nm, labeled aside) and different core sharpness with SI = 0.83 (A), 0.68 (B), and 0.32 (C). (**D**) Histogram of strain measurements in Pd shells from the samples in (A) to (C) with thickness increasing top to bottom. Bulk Pd lattice is used as the reference. (**E**) Average shell strain with increasing shell thickness for three core geometries. (**F**) Critical thickness of core-shell $Au_{cube}@Pd_{cube}$ NPs depending on the core sharpness and particle size.

particles (SI = 0.83), the Pd shell maintained a coherent lattice with the Au core for all thickness values explored (Fig. 2A, bulk Au lattice used as the reference). However, with increasingly rounded cores (SI = 0.68 and 0.32), strain release in the Pd occurs in thinner shells (Fig. 2, B and C). Histograms of the actual shell strain (bulk Pd lattice used as the reference) in each of these samples further confirms that sharp-tipped cores stabilize strained shells compared to traditional rounded particles (Fig. 2D).

Together, these data allow for quantification of the critical thickness as a function of particle morphology. Here, the thickness specifically refers to the Pd shell thickness on {100} facets. By measuring strain in NPs with different Pd shell thicknesses (1 to 25 nm) for each core geometry (SI = 0.83, 0.68, and 0.32), a sigmoidal relationship between Pd strain and shell thickness is observed (Fig. 2E). For each geometry, we collected >20 datapoints to ensure a high degree of statistical significance (raw data shown in fig. S9 to S11). We used the half maximum of the second derivative from these sigmoidal strain plots (defined in fig. S12) to identify the initiation of strain relaxation. A threshold value of 4.1% strain in the shell is observed for each system and the Pd shell thickness at which this occurs represents the critical thickness for the core-shell $Au_{cube}@Pd_{cube}$ NPs. The measured critical thickness for rounded cores (SI = 0.32) is 3.1 nm, consistent with previously reported values (*11*, *12*). However, for sharper cores (SI = 0.68 and 0.83), the critical thickness increases to 6.8 and 11.3 nm. This increase in critical thickness with SI value signifies that control over morphology can be used to stabilize epitaxial strain (as shown in Fig. 2F). Measuring the critical thickness for particles with core sizes of 30 and 20 nm (fig. S13) shows that this finding tends to be independent of particle size and is very likely a geometric effect. However, achieving ultrasharp cores (SI > 0.8) for 30 and 20 nm core-size particles poses a large challenge. A trade-off emerges between particle size and strain stability, with smaller NPs offering more surface area, while larger NPs exhibit a more stable surface strain.

To understand how core geometry facilitates surface strain preservation, we use molecular dynamics (MD) simulations to replicate the layer-by-layer synthesis of core-shell $Au_{cube}@Pd_{cube}$ structures with both sharp and round Au cores (see details of the simulations in Materials and Methods). The results of the whole-particle MD simulations show that dislocations nucleate around the corners but at different shell thicknesses for sharp- and round-core cases. In sharp-core particles, the first dislocation nucleates at a 5 nm shell thickness (Fig. 3A), whereas rounded particles trigger nucleation with a much thinner Pd shell (<1 nm) (Fig. 3B). With an increase in shell thickness, dislocations propagated and multiplied more in round-core particles (refer to Supplementary Movies). The calculated dislocation density is low in sharp-core $Au_{cube}@Pd_{cube}$ NPs even beyond 9 nm of Pd shell, while round-core $Au_{cube}@Pd_{cube}$ NPs exhibit a considerably higher dislocation density when the shell grows beyond 1 nm (Fig. 3C). The longitudinal surface strain starts to drop in the round-core particles when the dislocation density increases, indicating that dislocations facilitate surface strain

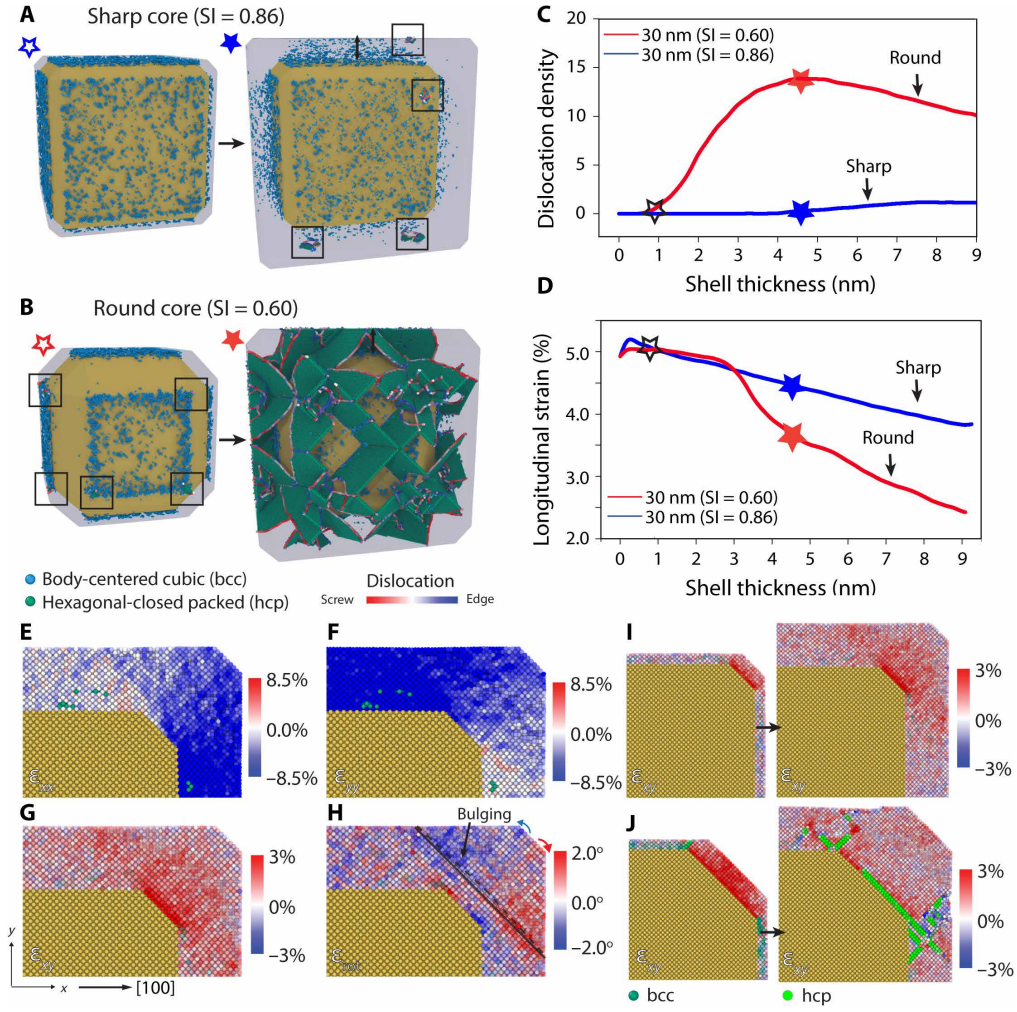

Fig. 3. MD simulation of dislocation nucleation. (**A** and **B**) 3D views of core-shell $Au_{cube}@Pd_{cube}$ MD simulations with different shell thicknesses (1.0 and 5.0 nm) and different core sharpnesses [SI = 0.86 (A) and 0.60 (B)]. Local regions with body-centered cubic (bcc) coordination (blue)indicate large structural deformation of the face-centered cubic (fcc) lattice according to the Bain transformation path model. Regions with hexagonal-close packed (hcp) coordination (green) indicate stacking faults that form as a result of dislocations splitting into partial dislocations. (**C**) Dislocation density (total length over volume) as a function of the shell thickness from MD simulations. (**D**) Average longitudinal strain (ε_{xx}) at the center of the particles' facets in a radius of 5 nm. (**E** to **H**) Strain maps of a slice through a simulation snapshot for a $Au_{cube}@Pd_{cube}$ NP (SI = 0.86) with ~4 nm shell thickness. In (H), the dotted line traces the atomic column, which deviates from a straight line (solid), indicating the lattice bulging. The red and blue arrows in (H) indicate clockwise and counterclockwise rotation, respectively. (**I** and **J**) Shear maps from simulation snapshots from sharp (SI = 0.86) (I) and truncated (SI = 0.60) (J) NPs at a thin (~1 nm) and thick (~4 nm) shell thickness. Shear and rotation maps are averaged over five subslices to reduce noise.

relaxation (Fig. 3D). These results show that misfit dislocations form more easily in round-core NPs.

Previous studies have attributed the dislocation formation in face-centered cubic (fcc) metal heterointerfaces to intensive local shear (*26*). In core-shell geometries, large shear stress has been predicted to concentrate at the corners, which causes bulging of atomic planes and later slip to form dislocations in the shell (*11*). Our MD simulations also revealed that the Poisson effect from the Pd shell at {100} facets exert compressive stress on the corner regions (Fig. 3, E and F), leading to localized lattice shear (Fig. 3G) and abovementioned lattice bulging (Fig. 3F) at the corners. The simulated kinetics also show that dislocations initiate from a void in the surface lattice plane, triggering the formation of a stacking fault bounded by partial dislocations (fig. S14). To understand the effect of corner sharpness on shear stress, strain profiles from sharp- and round-core core-shell NPs with different shell thickness have been simulated (fig. S15). We compared the local shear strain of sharp- and round-core NPs (Fig. 3, I and J), and the results highlight larger shear strain at the corners in the truncated case, which later causes lattice slipping and stacking fault formation. In contrast, the sharp-core case has weaker shear strain, allowing the shell to grow thicker without dislocation nucleation.

To test the stability of surface strain in core-shell Au@Pd NPs, we performed Suzuki-type homocoupling reactions (*27*) using *trans*-2-phenylvinylboronic acid (PVBA) as a substrate and sharp-core or round-core core-shell $Au_{cube}@Pd_{cube}$ NPs as nanocatalysts. In this class of reactions (*28*–*30*), Pd undergoes leaching and oxidation into PdO_x species during the catalytic process, followed by redeposition after formation of new carbon-carbon bonds (Fig. 4A) (*31*–*35*). Previous results indicate this reaction is favored with Pd {100} facets

(*36*) under tensile strain (*37*, *38*), but the catalytic conditions involve alkaline conditions and an elevated temperature of 80°C, which can lead to catalyst deactivation. Consequently, establishing more stable strain states in Pd surfaces would improve the activity and recyclability of catalysts for this heterogeneous reaction (*28*, *29*, *39*).

To evaluate the strain stability during the catalytic homocoupling, we assessed the strain profile of multiple $Au_{cube}@Pd_{cube}$ NPs before and after the reaction (fig. S16). The results reveal that the sharp-core NPs maintain the epitaxial strain in the shell after the reaction, whereas the strain in round-core NPs is largely released, presumably through the introduction of dislocations (Fig. 4B). We evaluated the activity of the core-shell Au@Pd nanocatalysts by monitoring the reaction kinetics via ultraviolet-visible (UV-vis) spectrophotometry. In this system, the homocoupling products of PVBA are *trans,trans*-1,4-diphenyl-1,3-butadiene (DPBT), which is spectroscopically active with a pronounced absorption peak at $\lambda_{max} = 348$ nm (calculated in fig. S17A). By monitoring the absorbance of this peak over time, we obtain reaction kinetics for both sharp-core and round-core $Au_{cube}@Pd_{cube}$ NPs (Fig. 4C). The kinetic profiles show that nanocatalysts with sharp Au cores exhibited a larger slope during the first 2 hours, indicating a higher catalytic reaction rate in comparison to that of the round-core case. The reactivities of the different Pd shells were determined by comparing the initial reaction rate (*27*) (γ_0), calculated based on the extinction coefficient of the DPBT (fig. S17B; see Materials and Methods). Both pure Pd cubes (unstrained, no Au core) and round-core $Au_{cube}@Pd_{cube}$ particles above the critical thickness exhibit similar activity due to the relaxed strain in the shell (Fig. 4D). In contrast, the sharp-core $Au_{cube}@Pd_{cube}$ nanocatalysts demonstrate an activity (6.3×10^9 M $min^{-1} m_{Pd}^{-2}$) that is 4.3-fold higher than that for round-core $Au_{cube}@Pd_{cube}$ (1.5×10^9 M $min^{-1} m_{Pd}^{-2}$) and 5.3-fold higher than pure unstrained Pd cubes (1.2×10^9 M $min^{-1} m_{Pd}^{-2}$; Fig. 4D). These results confirm that lattice strain stabilized by core-sharpening enhances the reactivity of catalytic surfaces.

Furthermore, we conduct a comparison of the product yields between sharp-core and round-core $Au_{cube}@Pd_{cube}$ NP catalysts. Whereas the DPBT yield reaches 74.3% for round-core $Au_{cube}@Pd_{cube}$ NPs it is 96.8% with particles synthesized with a sharp core

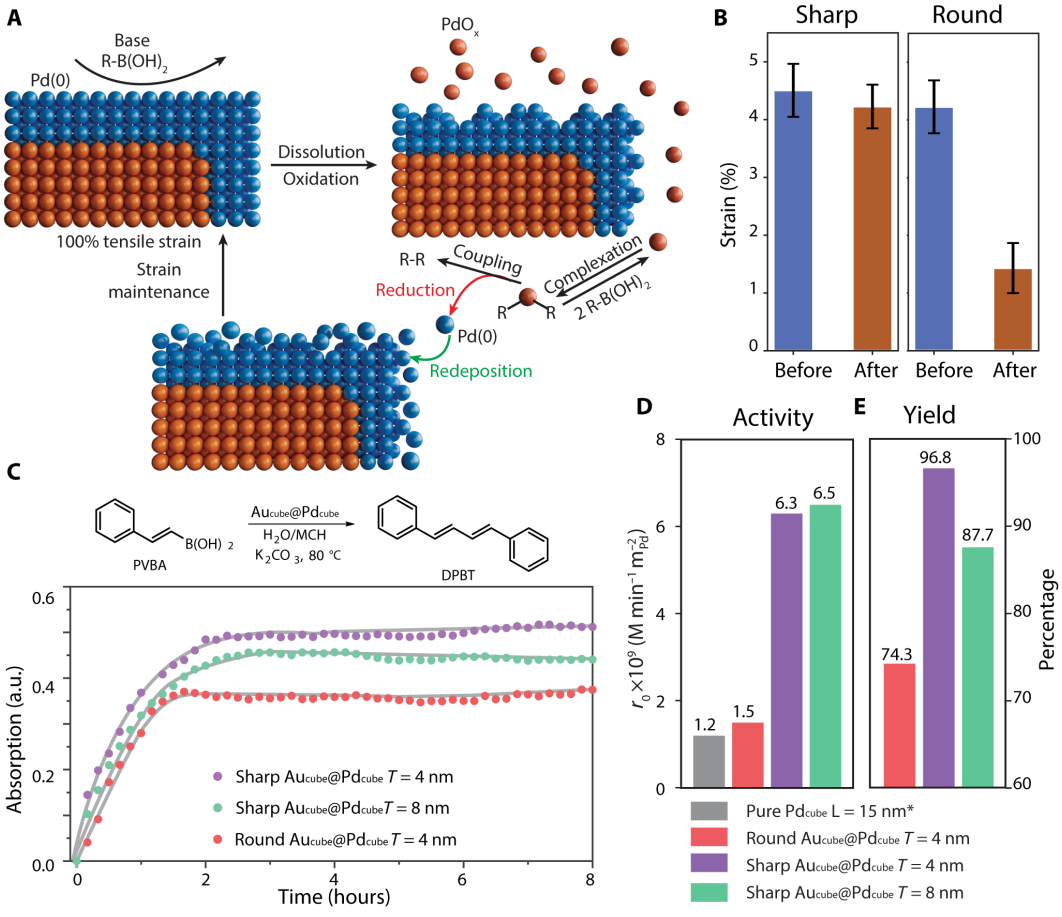

Fig. 4. Strain stability under catalytic reactions. (**A**) Schematic illustration of the catalytic process of homocoupling in a Suzuki-type reaction on sharp-core core-shell $Au_{cube}@Pd_{cube}$ NPs with tensile strain. This type of reaction relies on the dissolution, reduction, and redeposition of Pd, which presents a harsh environment for strain-engineered catalysts. (**B**) The average strain in sharp- and round-core $Au_{cube}@Pd_{cube}$ NPs with a 4 nm shell thickness before and after the catalytic reaction. (**C**) The kinetic profiles of homocoupling reactions from $Au_{cube}@Pd_{cube}$ catalysts with sharp (purple and green) and round cores (red). Top: schematic of homocoupling reaction catalyzed by Pd surfaces. (**D**) Comparison of the catalytic activities of pure Pd_{cube} particles (gray) (*27*) with round-core (red) and sharp-core (purple and green) $Au_{cube}@Pd_{cube}$ nanocatalysts. The rate is normalized by the surface area of Pd. (**E**) Comparison of the yield between round-core (red) and sharp-core (purple and green) $Au_{cube}@Pd_{cube}$ nanocatalysts.

(Fig. 4E). In addition, by increasing the thickness of the Pd shell in sharp-core $Au_{cube}@Pd_{cube}$ NPs (from 4 to 8 nm), the activity and yield remain comparable to the 4-nm sharp-core catalysts (Fig. 4, D and E, green). This observation shows that even with a thicker shell (and greater catalytic surface area per particle), the surface strain of sharp-core core-shell particles remain stable under reaction conditions.

DISCUSSION

In summary, we introduce a morphology-control strategy aimed at stabilizing the surface strain of core-shell nanocatalysts. This approach increases the critical thickness in core-shell $Au_{cube}@Pd_{cube}$ systems when the core morphology is sharper. It accomplishes this by inhibiting dislocation nucleation at the particle corners, which in turn preserves the surface strain. Given that morphology control is more straightforward than consistently producing ultrathin shells, our work presents a promising method to streamline the synthesis of strain-engineered nanocatalysts with enhanced performance, potentially enabling their large-scale production. This finding holds promise for generalization to other core-shell NPs and even other nano-architectured materials, offering additional opportunities for strain engineered structures.

MATERIALS AND METHODS

Materials synthesis

Chemical reagents

Hydrogen tetrachloroaurate trihydrate ($HAuCl_4$; 99.999% trace metal basis), L-ascorbic acid (AA), sodium borohydride ($NaBH_4$), silver nitrate ($AgNO_3$; 99.999% trace metal basis), palladium chloride ($PdCl_2$; 99.999%), potassium bromide (KBr), potassium carbonate (K_2CO_3), PVBA, DPBT, hydrogen chloride (37 wt %, 12.1 M), methylcyclohexene (MCH), chloroform are all purchased from Sigma-Aldrich. Hexadecyltrimethylammonium bromide (CTAB) and hexadecyltrimethylammonium chloride (CTAC) were purchased from TCI America. All reagents are used as received. Milli-Q water (0.22 μM pore size, 18.2 megohm · cm at 25°C) was used for all syntheses and before each growth all glassware were treated with aqua regia and rinsed with excess water.

Synthesis of Au clusters

First, $HAuCl_4 \cdot 3H_2O$ solution (10 mM, 250 μl) and 5 ml of 0.2 M CTAB solution are added to 4.75 ml of water. Next 0.6 ml of freshly made ice-cold 10 mM $NaBH_4$ solution was quickly injected into the above solution under vigorous stirring. The solution color changed from yellow to brownish, indicating the formation of gold clusters (*40*). After vigorously stirring for 2 min and the obtained solution was aged at 27°C for 3 hours before use.

Synthesis of 10-nm Au seeds

Similar to our previously reported works (*41*, *42*), aqueous solutions of CTAC (200 mM, 2 ml), AA (100 mM, 1.5 ml), and an aqueous $HAuCl_4$ solution (0.5 mM, 2 ml) were mixed, followed by one-shot injection of the above Au clusters (50 μl). The reaction was allowed to continue at 27°C for 15 min. The product was collected by centrifugation at 21,000 rcf for 90 min, and then washed with water once for further use and characterization.

Synthesis of sharp Au cubes

In a typical synthesis of 50-nm gold nanocubes with high sharpness, an aqueous solution containing CTAC (50 mM, 12 ml), KBr (100 mM, 12 μl), and AA (100 mM, 39 μl) was mixed with 10-nm Au seeds [3.406 optical density (OD), 14.5 μl] thoroughly. Afterward, an aqueous $HAuCl_4$ solution (10 mM, 0.3 ml) was added and then kept at room temperature for 3 hours to finish the reaction. It is noteworthy to mention that the size of Au cube NPs can be tuned by the amounts of seeds. By adjusting the ratio between growth solution (Au^{3+}) and seeds (Au^0) added in the solution, we can achieve different particle sizes. The higher the Au^{3+}/Au^0 ratio is, the larger particle can be achieved. The size variation of the Au cubes is less than 4% (fig. S18). In addition, the sharpness can be controlled by changing the concentration of bromide ion in the growth solution, which is independent from the size control. After reaction completion, the obtained Au cube NPs were centrifuged at 6000 rcf for 12 min and washed with water once. The obtained pellet was redispersed in 2 ml of water for future use.

Synthesis of rounded Au cubes

In a typical synthesis of 50-nm gold nanocubes with rounded tips and edges, two steps are involved. First, 10-nm Au seeds (3.406 OD, 14.5 μl) were grown into larger seeds by addition to a growth solution containing CTAC (200 mM, 1.4 ml), H_2O (1.33 ml), AA (100 mM, 1.05 ml), and $HAuCl_4$ (10 mM, 70 μl). After mixing thoroughly, this solution was maintained at room temperature for 30 min and then centrifuged at 10000 rcf for 15 min to get pellets. Afterward, the pellet was suspended in CTAC (50 mM, 1.5 ml), to which, KBr (100 mM, 3 μl), AA (100 mM, 3.9 μl), and $HAuCl_4$ (10 mM, 30 μl) were added to get rounded cube NPs with blunt tips.

Preparation of H_2PdCl_4 solution

The H_2PdCl_4 (10 mM) was prepared by mixing $PdCl_2$ (44.5 mg) into HCl (0.02 M, 25 ml) aqueous solution under stirring at 50°C until complete dissolution.

Synthesis of core-shell $Au_{cube}@Pd_{cube}$ NPs with different Pd thickness

To control the epitaxial overgrowth of core-shell $Au_{cube}@Pd_{cube}$ NPs, the Au cube NP solution (4.86 OD, 500 μl) was added to a growth solution containing CTAB (40 mM, 1 ml), H_2PdCl_4 (10 mM, 40 μl), and AA (100 mM, 9 μl) and then heated at 60°C for 3 hours. Similarly, the thickness of the Pd shell can be tuned by changing the ratio between growth solution to Au cube NPs keeping all other conditions the same.

Preparation $Au_{cube}@Pd_{cube}$ catalyst

In a typical synthesis of sharp $Au_{cube}@Pd_{cube}$, sharp Au cubes were first obtained with abovementioned methods. As a reference, the concentration of NP was determined by the UV-vis spectrum (λ_{max} = 556 nm, 4.2 OD, 2 ml). To form $Au_{cube}@Pd_{cube}$ NPs, to the above Au cube solution, a Pd growth solution was added containing CTAB (40 mM, 3.6 ml), H_2PdCl_4 (10 mM, 200 μl), and AA (100 mM, 45 μl), which was heated at 60°C for 3 hours. After completing the growth, it was centrifuged at 5000 rcf for 5 min to get pellets and the particles were washed with water once to remove any remaining reagent that may affect the catalytic test. Afterward, the obtained solution was carefully transferred into 1.5-ml centrifuge tubes and washed with relatively low centrifugation speed (4000 rcf, 3 min). The supernatant was carefully removed and then all the particles were resuspended in 200 μl of water for future use. To control the thickness of the Pd shell, a different amount of Pd growth solution was added to the Au cube solution. Similarly, for the rounded $Au_{cube}@Pd_{cube}$ NPs, a similar growth procedure was used to control the Pd thickness except replacing the sharp Au cube solution with one with truncated Au cubes.

4D-STEM strain mapping

EMPAD data acquisition

The 4D-STEM datasets were taken on an aberration-corrected Thermo Fisher Titan Themis at 300 keV with an EMPAD. A 1.76-mrad convergence angle was used, leading to a 0.69 nm probe size (defined by full width half maximum probe diameter). The camera length is 185 mm to capture more higher-order diffraction spots for the EWPC method. For a 300-kV electron beam, 579 ADUs represent one electron per pixel. For all the datasets, an exposure time of 1.86 ms per frame (1 ms acquisition time along with 0.86 ms readout time) was used when acquiring the EMPAD 4D datasets. The scan size in real space (the number of pixels the beam scans across) can be set from 64 × 64 to 512 × 512. The scan size of the data used in this work was 256 × 256. The total time for capturing one 4D data was 122 s.

Strain mapping

The EWPC method is used to measure the strain profiles of the core-shell nanocubes. The workflow of EWPC method is shown in fig. S2A. The raw diffraction pattern (fig. S2B) is first transformed to logarithmic scale (fig. S2C) and then a Gaussian mask (fig. S2D) is applied on it to reduce the boundary effects (fig. S2E). The power cepstrum image is acquired through fast-Fourier transform of the diffraction (fig. S2F). The cepstrum spot positions are measured through the center of mass method to determine the two lattice vectors along x and y directions. The strain profiles, including e_{xx}, e_{yy}, and e_{xy}, and rotation can be calculated through polar decomposition method. The strain maps in Fig. 2 (A to C) average edges with similar thickness (variance <1 nm) to improve the signal-to-noise ratio.

The averaged lattice constant of center Au core region is used as the reference of the strain map. When the Pd shell is thin and strained, the center region reference is regarded as the lattice constant of bulk Au (4.078 Å). When the Pd shell is thick and the strain is released, the center region is regarded as an overlay of bulk Au and Pd lattice, owing to the projection effects from the transmitted electron beam. Therefore, we perform the strain correction method shown in fig. S3. The center diffraction and cepstrum is expressed as the Au + x * Pd (fig. S3A), where the coefficient x is decided by the thickness and strain of the Pd shell. We calculate the diffraction difference between cepstrum of the center Au region and Pd shell (fig. S3B), where a dipole shows at each cepstrum spot (fig. S3C). The blue and red contrast in the dipole represent the Au and Pd lattice, respectively (fig. S3D). Through tuning the coefficient (x) of the cepstrum from the Pd shell, the Pd peak intensity in the dipoles at cepstrum spots reduces (fig. S3E). The coefficient (0.11), which gives the zero Pd peak intensity, are chosen to correct the cepstrum in the Au region for a more precise strain mapping. After the correction, the lattice constant in the center region of the thick Pd shell particle can also be regarded as the bulk Au lattice constant.

To determine the critical thickness, the shell strain and shell thickness are measured statistically from a number of core-shell NPs with different thickness and core sharpness. All measured data points are displayed in fig. S9. The shell strain-thickness scattered plots are fitted by sigmoid functions, which is a commonly used "S shape" function. The expression is the following

$$\epsilon = 4.8\% \times \frac{1}{1 + e^{0.5(t-c)}} + 4.8$$

where ϵ is the shell strain and the t is shell thickness. 4.8% is the difference between the unstrained Au and Pd lattice. By performing the least square fitting of the scattered datapoints to the sigmoid function, the parameter c, which represent the center of the sigmoid function, can be determined for each core-sharpness NPs. The derivations of the fitted curves are calculated and shown as the colored shadows in fig. S9. The thickness at the half of the minimum derivation points is chosen as the critical thickness where the strain starts to release (as shown in fig. S12).

MD simulation

Seed atomistic models are generated from an infinite fcc lattice with cell parameter 4.08 Å by selecting all lattice sites that fall within the outline of the NP. These sites are occupied with Au and Pd atoms according to the core-shell nanostructure geometry. Atoms in the Pd shell are sorted into concentric monolayers (fig. S19A). Layers are successively added to the MD model in a series of simulation stages, reproducing the kinetics of Pd shell growth onto the Au core (fig. S19, B and C). The model is simulated with classical MD using the LAMMPS software package (*43*). Atom velocities are sampled from the Maxwell-Boltzmann distribution at temperature of 300 K. Interatomic potentials are computed with the long-range generalized form of the embedded-atom method of Finnis and Sinclair using the quantum Sutton-Chen force field (*44*–*48*). During each deposition stage, the MD models are relaxed for 0.1 ns at 300 K using a Langevin thermostat with a dumping constant of 0.0020 fs and a 1 fs time integration in the microcanonical ensemble (*49*).

After energy minimization of the Au core, Pd layers are deposited layer by layer onto the surface of the MD models while keeping the atom dynamics in equilibration. The procedure to grow the Pd shell by one layer is as follows: First, a new Pd layer is created surrounding the existing NP. To mimic the effect of the bromide concentration in experiment, we temporarily include an auxiliary Pd layer on the outside of the new Pd layer (fig. S19B). This auxiliary Pd layer ensures stability of the NP surface by suppressing diffusion of Pd atoms during deposition. Its presence reproduces the even and smooth surface growth observed in experiment as a consequence of the presence of bromide. Second, all Pd atoms of the new layer are moved radially from their initial positions toward the NP center up to a minimum distance of 3 Å from any previously equilibrated atom. Atoms in the auxiliary layer are also moved radially up to a minimum distance of 2 Å from the atoms in the new layer. The smaller cutoff distance promotes inward dynamics of the atoms improving deposition kinetics. Third, the system is equilibrated using MD simulation. Fourth, the atoms of the auxiliary layer are removed from the simulation (fig. S19C).

Snapshots of the MD simulation are recorded at 10 ps time intervals. The symmetric and antisymmetric strain components are computed from the strain tensor measured with the cell deformation method (*50*, *51*). The OVITO software package is used to render the MD snapshots, to identify the local structure coordination, and to measure the dislocation density (*52*–*56*).

Catalytic reaction

To test the catalytic activities of both sharp and round Au_{cube}@Pd_{cube} particles, the PVBA homocoupling reaction was performed in both cases. To determine the reaction kinetics of this reaction, PVBA, K_2CO_3, water and MCH were first transferred into a quartz cuvette with an optical path of 10 mm. This cuvette is loaded into a preheated UV-vis stage (80°C) for 10 min before adding Au@Pd catalysts (50 μl), which are prepared according to the previous section. All the catalytic measurements were conducted with the condition as follows: [PVBA] = 0.40 mM and [K_2CO_3] = 2.00 mM, in

water/MCH (1/1) biphasic medium. The reaction kinetics of the PVBA homocoupling were investigated by monitoring the appearance of the product (DPBT) at a wavelength of 348 nm with UV-vis spectrophotometry. The reactivity of the catalyst is determined by the initial reaction rate γ_0, which is determined by the first two points in the plot and normalized by the total surface area of the Pd cube. The yield is determined by normalizing the equilibrium adsorption intensity with the theoretical adsorption of the DPBT.

Supplementary Materials

The PDF file includes:
Figs. S1 to S19
Legends for movies S1 and S2

Other Supplementary Material for this manuscript includes the following:
Movies S1 and S2

REFERENCES AND NOTES

1. M. K. Debe, Electrocatalyst approaches and challenges for automotive fuel cells. *Nature* **486**, 43–51 (2012).
2. H. Wang, S. Xu, C. Tsai, Y. Li, C. Liu, J. Zhao, Y. Liu, H. Yuan, F. Abild-Pedersen, F. B. Prinz, J. K. Nørskov, Y. Cui, Direct and continuous strain control of catalysts with tunable battery electrode materials. *Science* **354**, 1031–1036 (2016).
3. M. Luo, S. Guo, Strain-controlled electrocatalysis on multimetallic nanomaterials. *Nat. Rev. Mater.* **2**, 17059 (2017).
4. L. Bu, N. Zhang, S. Guo, X. Zhang, J. Li, J. Yao, T. Wu, G. Lu, J.-Y. Ma, D. Su, X. Huang, Biaxially strained PtPb/Pt core/shell nanoplate boosts oxygen reduction catalysis. *Science* **354**, 1410–1414 (2016).
5. T. He, W. Wang, F. Shi, X. Yang, X. Li, J. Wu, Y. Yin, M. Jin, Mastering the surface strain of platinum catalysts for efficient electrocatalysis. *Nature* **598**, 76–81 (2021).
6. D. Wang, H. L. Xin, R. Hovden, H. Wang, Y. Yu, D. A. Muller, F. J. DiSalvo, H. D. Abruña, Structurally ordered intermetallic platinum–cobalt core–shell nanoparticles with enhanced activity and stability as oxygen reduction electrocatalysts. *Nat. Mater.* **12**, 81–87 (2013).
7. V. R. Stamenkovic, B. S. Mun, M. Arenz, K. J. J. Mayrhofer, C. A. Lucas, G. Wang, P. N. Ross, N. M. Markovic, Trends in electrocatalysis on extended and nanoscale Pt-bimetallic alloy surfaces. *Nat. Mater.* **6**, 241–247 (2007).
8. C. Cui, L. Gan, M. Heggen, S. Rudi, P. Strasser, Compositional segregation in shaped Pt alloy nanoparticles and their structural behaviour during electrocatalysis. *Nat. Mater.* **12**, 765–771 (2013).
9. J. W. Matthews, A. E. Blakeslee, Defects in epitaxial multilayers: I. Misfit dislocations. *J. Cryst. Growth* **27**, 118–125 (1974).
10. J. T. L. Gamler, A. Leonardi, X. Sang, K. M. Koczkur, R. R. Unocic, M. Engel, S. E. Skrabalak, Effect of lattice mismatch and shell thickness on strain in core@shell nanocrystals. *Nanoscale Adv.* **2**, 1105–1114 (2020).
11. M. Nathanson, K. Kanhaiya, A. Pryor, J. Miao, H. Heinz, Atomic-scale structure and stress release mechanism in core–shell Nanoparticles. *ACS Nano* **12**, 12296–12304 (2018).
12. N. Bhattarai, G. Casillas, A. Ponce, M. Jose-Yacaman, Strain-release mechanisms in bimetallic core–shell nanoparticles as revealed by Cs-corrected STEM. *Surf. Sci.* **609**, 161–166 (2013).
13. H. L. Xin, J. A. Mundy, Z. Liu, R. Cabezas, R. Hovden, L. F. Kourkoutis, J. Zhang, N. P. Subramanian, R. Makharia, F. T. Wagner, D. A. Muller, Atomic-resolution spectroscopic imaging of ensembles of nanocatalyst particles across the life of a fuel cell. *Nano Lett.* **12**, 490–497 (2012).
14. X. Wang, S.-I. Choi, L. T. Roling, M. Luo, C. Ma, L. Zhang, M. Chi, J. Liu, Z. Xie, J. A. Herron, M. Mavrikakis, Y. Xia, Palladium–platinum core-shell icosahedra with substantially enhanced activity and durability towards oxygen reduction. *Nat. Commun.* **6**, 7594 (2015).
15. J. E. S. van der Hoeven, J. Jelic, L. A. Olthof, G. Totarella, R. J. A. van Dijk-Moes, J.-M. Krafft, C. Louis, F. Studt, A. van Blaaderen, P. E. de Jongh, Unlocking synergy in bimetallic catalysts by core–shell design. *Nat. Mater.* **20**, 1216–1220 (2021).
16. Y. Chen, J. Pei, Z. Chen, A. Li, S. Ji, H. Rong, Q. Xu, T. Wang, A. Zhang, H. Tang, J. Zhu, X. Han, Z. Zhuang, G. Zhou, D. Wang, Pt atomic layers with tensile strain and rich defects boost ethanol electrooxidation. *Nano Lett.* **22**, 7563–7571 (2022).
17. X. Yang, J. H. Lee, S. Kattel, B. Xu, J. G. Chen, Tuning reaction pathways of electrochemical conversion of CO2 by growing Pd shells on Ag nanocubes. *Nano Lett.* **22**, 4576–4582 (2022).
18. G. Wu, X. Han, J. Cai, P. Yin, P. Cui, X. Zheng, H. Li, C. Chen, G. Wang, X. Hong, In-plane strain engineering in ultrathin noble metal nanosheets boosts the intrinsic electrocatalytic hydrogen evolution activity. *Nat. Commun.* **13**, 4200 (2022).
19. M. Xie, Z. Lyu, R. Chen, M. Shen, Z. Cao, Y. Xia, Pt–Co@Pt octahedral nanocrystals: Enhancing their activity and durability toward oxygen reduction with an intermetallic core and an ultrathin shell. *J. Am. Chem. Soc.* **143**, 8509–8518 (2021).
20. M. J. Hÿtch, E. Snoeck, R. Kilaas, Quantitative measurement of displacement and strain fields from HREM micrographs. *Ultramicroscopy* **74**, 131–146 (1998).
21. C. Ophus, Four-dimensional scanning transmission electron microscopy (4D-STEM): From scanning nanodiffraction to ptychography and beyond. *Microsc. Microanal.* **25**, 563–582 (2019).
22. Y. Han, K. Nguyen, M. Cao, P. Cueva, S. Xie, M. W. Tate, P. Purohit, S. M. Gruner, J. Park, D. A. Muller, Strain mapping of two-dimensional heterostructures with subpicometer precision. *Nano Lett.* **18**, 3746–3751 (2018).
23. M. W. Tate, P. Purohit, D. Chamberlain, K. X. Nguyen, R. Hovden, C. S. Chang, P. Deb, E. Turgut, J. T. Heron, D. G. Schlom, D. C. Ralph, G. D. Fuchs, K. S. Shanks, H. T. Philipp, D. A. Muller, S. M. Gruner, High dynamic range pixel array detector for scanning transmission electron microscopy. *Microsc. Microanal.* **22**, 237–249 (2016).
24. E. Padgett, M. E. Holtz, P. Cueva, Y.-T. Shao, E. Langenberg, D. G. Schlom, D. A. Muller, The exit-wave power-cepstrum transform for scanning nanobeam electron diffraction: Robust strain mapping at subnanometer resolution and subpicometer precision. *Ultramicroscopy* **214**, 112994 (2020).
25. J.-E. Park, Y. Lee, J.-M. Nam, Precisely shaped, uniformly formed gold nanocubes with ultrahigh reproducibility in single-particle scattering and surface-enhanced raman scattering. *Nano Lett.* **18**, 6475–6482 (2018).
26. R. F. Zhang, J. Wang, I. J. Beyerlein, T. C. Germann, Dislocation nucleation mechanisms from fcc/bcc incoherent interfaces. *Scr. Mater.* **65**, 1022–1025 (2011).
27. W. C. Elias, A. M. Signori, L. Zaramello, B. L. Albuquerque, D. C. de Oliveira, J. B. Domingos, Mechanism of a Suzuki-type homocoupling reaction catalyzed by palladium nanocubes. *ACS Catal.* **7**, 1462–1469 (2017).
28. D. Astruc, F. Lu, J. R. Aranzaes, Nanoparticles as recyclable catalysts: The frontier between homogeneous and heterogeneous catalysis. *Angew. Chem. Int. Ed.* **44**, 7852–7872 (2005).
29. A. Fihri, M. Bouhrara, B. Nekoueishahraki, J.-M. Basset, V. Polshettiwar, Nanocatalysts for Suzuki cross-coupling reactions. *Chem. Soc. Rev.* **40**, 5181–5203 (2011).
30. Y. Zhu, N. S. Hosmane, Nanocatalysis: Recent advances and applications in boron chemistry. *Coord. Chem. Rev.* **293-294**, 357–367 (2015).
31. H. Lakmini, I. Ciofini, A. Jutand, C. Amatore, C. Adamo, Pd-Catalyzed homocoupling reaction of arylboronic acid: Insights from density functional theory. *J. Phys. Chem. A* **112**, 12896–12903 (2008).
32. C. Adamo, C. Amatore, I. Ciofini, A. Jutand, H. Lakmini, Mechanism of the palladium-catalyzed homocoupling of arylboronic acids: Key involvement of a palladium peroxo complex. *J. Am. Chem. Soc.* **128**, 6829–6836 (2006).
33. M. C. D'Alterio, È. Casals-Cruañas, N. V. Tzouras, G. Talarico, S. P. Nolan, A. Poater, Mechanistic aspects of the palladium-catalyzed Suzuki-Miyaura cross-coupling reaction. *Chem. A Eur. J.* **27**, 13481–13493 (2021).
34. A. K. Diallo, C. Ornelas, L. Salmon, J. R. Aranzaes, D. Astruc, "Homeopathic" catalytic activity and atom-leaching mechanism in Miyaura-Suzuki reactions under ambient conditions with precise dendrimer-stabilized Pd nanoparticles. *Angew. Chem. Int. Ed.* **46**, 8644–8648 (2007).
35. M. Pérez-Lorenzo, Palladium nanoparticles as efficient catalysts for Suzuki cross-coupling reactions. *J. Phys. Chem. Lett.* **3**, 167–174 (2012).
36. G. Collins, M. Schmidt, C. O'Dwyer, J. D. Holmes, G. P. McGlacken, The origin of shape sensitivity in palladium-catalyzed Suzuki–Miyaura cross coupling reactions. *Angew. Chem. Int. Ed.* **53**, 4142–4145 (2014).
37. J. Fan, H. Du, Y. Zhao, Q. Wang, Y. Liu, D. Li, J. Feng, Recent progress on rational design of bimetallic Pd based catalysts and their advanced catalysis. *ACS Catal.* **10**, 13560–13583 (2020).
38. D. Y. Kim, K. W. Choi, X.-L. Zhong, Z.-Y. Li, S. H. Im, O. O. Park, Au@Pd core–shell nanocubes with finely-controlled sizes. *CrstEngComm* **15**, 3385–3391 (2013).
39. R. Narayanan, M. A. El-Sayed, Effect of catalysis on the stability of metallic nanoparticles: Suzuki reaction catalyzed by PVP-palladium nanoparticles. *J. Am. Chem. Soc.* **125**, 8340–8347 (2003).
40. L. Qiao, N. Pollard, R. D. Senanayake, Z. Yang, M. Kim, A. S. Ali, M. T. Hoang, N. Yao, Y. Han, R. Hernandez, A. Z. Clayborne, M. R. Jones, Atomically precise nanoclusters predominantly seed gold nanoparticle syntheses. *Nat. Commun.* **14**, 4408 (2023).
41. Z. Cheng, M. R. Jones, Assembly of planar chiral superlattices from achiral building blocks. *Nat. Commun.* **13**, 4207 (2022).
42. Z. Cheng, M. R. Jones, Separation of nanoparticle seed pseudoisomers via amplification of their crystallographic differences. *J. Am. Chem. Soc.* **145**, 27702–27707 (2023).
43. S. Plimpton, Fast parallel algorithms for short-range molecular dynamics. *J. Comput. Phys.* **117**, 1–19 (1995).

44. M. S. Daw, M. I. Baskes, Embedded-atom method: Derivation and application to impurities, surfaces, and other defects in metals. *Phys. Rev. B* **29**, 6443–6453 (1984).
45. M. S. Daw, S. M. Foiles, M. I. Baskes, The embedded-atom method: A review of theory and applications. *Mater. Sci. Rep.* **9**, 251–310 (1993).
46. Y. Kimura, Y. Qi, T. Cagin, W. A. Goddard III, The quantum Sutton-Chen many-body potential for properties of fcc metals. *MRS Symposium Ser.* **554**, 43 (1999).
47. A. P. Sutton, J. Chen, Long-range Finnis–Sinclair potentials. *Philos. Mag. Lett.* **61**, 139–146 (1990).
48. H. Rafii-Tabar, A. P. Sulton, Long-range Finnis-Sinclair potentials for f.c.c. metallic alloys. *Philos. Mag. Lett.* **63**, 217–224 (1991).
49. T. Schneider, E. Stoll, Molecular-dynamics study of a three-dimensional one-component model for distortive phase transitions. *Phys. Rev. B* **17**, 1302–1322 (1978).
50. A. Leonardi, M. Leoni, M. Li, P. Scardi, Strain in atomistic models of nanocrystalline clusters. *J. Nanosci. Nanotechnol.* **12**, 8546–8553 (2012).
51. Y. Han, M.-Y. Li, G.-S. Jung, M. A. Marsalis, Z. Qin, M. J. Buehler, L.-J. Li, D. A. Muller, Sub-nanometre channels embedded in two-dimensional materials. *Nat. Mater.* **17**, 129–133 (2018).
52. A. Stukowski, Visualization and analysis of atomistic simulation data with OVITO–the open visualization tool. *Model. Simul. Mater. Sci. Eng.* **18**, 015012 (2010).
53. D. Faken, H. Jónsson, Systematic analysis of local atomic structure combined with 3D computer graphics. *Comput. Mater. Sci.* **2**, 279–286 (1994).
54. J. D. Honeycutt, H. C. Andersen, Molecular dynamics study of melting and freezing of small Lennard-Jones clusters. *J. Phys. Chem.* **91**, 4950–4963 (1987).
55. A. Stukowski, K. Albe, Extracting dislocations and non-dislocation crystal defects from atomistic simulation data. *Model. Simul. Mater. Sci. Eng.* **18**, 085001 (2010).
56. A. Stukowski, K. Albe, Dislocation detection algorithm for atomistic simulations. *Model. Simul. Mater. Sci. Eng.* **18**, 025016 (2010).

Acknowledgments: C.S., Z.C., and Y.H. acknowledge the use of Electron Microscopy Center (EMC) at Rice University. A.L. acknowledges Lilly Endowment Inc. through its support for the Indiana University Pervasive Technology Institute. **Funding:** The work is supported by NSF (CMMI-2239545). C.S. and Y.H. acknowledge the support from the Robert A. Welch Foundation (C-2065) and American Chemical Society Petroleum Research Fund (67236-DNI10). M.R.J. thanks the Robert A. Welch Foundation (C-2146), the David and Lucile Packard Foundation (2018-68049), and the American Chemical Society Petroleum Research Fund (65837-ND3). A.L. and M.E. acknowledge support from the Deutsche Forschungsgemeinschaft (DFG, German Research Foundation) Project-ID 452477982–LE4543/2-1. **Author contributions:** Conceptualization: M.R.J. and Y.H. Data curation: C.S., Z.C., and A.L. Methodology: C.S., Z.C., and A.L. Investigation: C.S., Z.C., and A.L. Visualization: C.S., Z.C., and A.L. Funding acquisition: M.E., M.R.J., and Y.H. Project administration: M.R.J. and Y.H. Supervision: M.E., M.R.J., and Y.H. Writing–original draft: C.S., Z.C., and Y.H. Writing–review and editing: C.S., Z.C., A.L., Y.Y., M.E., M.R.J., and Y.H. **Competing interests:** The authors declare that they have no competing interests. **Data and materials availability:** All data needed to evaluate the conclusions in the paper are present in the paper, Supplementary Materials, and https://zenodo.org/communities/hanlab-rice/.

Submitted 21 March 2024
Accepted 19 August 2024
Published 25 September 2024
10.1126/sciadv.adp3788